

Continuous Unitary Transformations using Tensor Network Representations Access the Full Many- Body Localized Spectrum

Qiyu Liu,^{1,*} Jan-Niklas Herre,² Dante M. Kennes,^{2,3,†} and Christoph Karrasch^{1,‡}

¹*Technische Universität Braunschweig, Institut für Mathematische Physik,
Mendelssohnstraße 3, 38106 Braunschweig, Germany*

²*Institute for Theory of Statistical Physics, RWTH Aachen University*

³*Max Planck Institute for the Structure and Dynamics of Matter,
Center for Free Electron Laser Science, Luruper Chaussee 149, 22761 Hamburg, Germany*

(Dated: March 16, 2026)

We develop variational continuous unitary transformations (VCUTs), which integrate Wegner-Wilson flow equations with tensor network techniques to approximately diagonalize many-body localized (MBL) Hamiltonians. The diagonalizing unitary is represented as a matrix product operator whose bond dimension controls the accuracy. For the disordered Heisenberg chain, VCUTs accurately reproduces the full spectrum across the ergodic-to-MBL crossover at small system sizes and scales to $L = 48$ sites. Beyond eigenenergies, the method can track the spatial entanglement structure of the diagonalizing unitary $U(l)$ at each flow step, enabling identification of local integrals of motion deep in the MBL phase.

I. INTRODUCTION

As one of the most intriguing phenomena in the field, many-body localization (MBL) is intrinsically different from Anderson localization due to its emergent integrability, which robustly prevents thermalization and conductivity even in the presence of interactions [1–8]. The fully many-body localized (fMBL) phase is characterized by a complete set of L quasilocal integrals of motion (LIOMs) $\{\tau_i^z\}_{i=1}^L$, known as l -bits [9, 10]. These l -bits can be constructed from the physical spin operators σ_i^z via a quasilocal unitary transformation U that diagonalizes the Hamiltonian \mathcal{H} : $\tau_i^z = U^\dagger \sigma_i^z U$. The operator U connects the physical basis to the l -bit basis in which the Hamiltonian takes a diagonal form:

$$\mathcal{H} = \sum_i h_i \tau_i^z + \sum_{i<j} J_{ij} \tau_i^z \tau_j^z + \dots, \quad (1)$$

where the couplings J_{ij} decay exponentially with distance $|i - j|$. As evident from this form, the l -bits are mutually commuting operators that also commute with \mathcal{H} , giving rise to the emergent integrability of the fMBL phase. Crucially, both U and the l -bits exhibit spatial locality: the l -bits are exponentially localized around their associated lattice sites, and U can be approximated by a finite-depth quantum circuit and admits an efficient MPO representation [11–13]. Consequently, applying U to the 2^L product states in the l -bit basis yields all eigenstates with area-law entanglement. Furthermore, the exponentially decaying interactions J_{ij} between l -bits lead to slow dephasing dynamics, which governs the spreading of local operators. In fMBL systems, a local operator spreads only logarithmically in time, $r \sim \xi \log(t)$, where ξ is the localization length [14–16]. In contrast, ergodic systems exhibit ballistic operator spreading, bounded by the Lieb-Robinson velocity [17], which sets the maximum speed at which information can propagate in systems with local interactions.

Verifying the existence of l -bits and understanding the ergodic-to-MBL transition requires probing the properties of highly excited eigenstates. This can be achieved either by computing eigenstates directly or by investigating the time evolution of many-body systems, which reveals whether a system thermalizes or not. Both approaches face significant challenges due to the exponential growth of the Hilbert space, severely limiting accessible time scales and system sizes.

Exact diagonalization (ED) provides numerically exact results but is limited to small system sizes ($L \lesssim 20$). The shift-and-invert technique [18] extends ED to larger systems ($L \lesssim 26$) by targeting eigenstates at specific energies. However, this method requires inverting the shifted Hamiltonian, typically performed via LU decomposition. Since the sparsity pattern of the Hamiltonian is not preserved during decomposition, the resulting memory overhead becomes the main bottleneck, and the method remains restricted to computing individual eigenstates rather than the full spectrum.

Tensor network methods offer an alternative route. DMRG-X [19] adapts the density matrix renormalization group to target highly excited eigenstates by exploiting their low entanglement in the MBL phase. However, the method requires a good initial guess and converges reliably only deep in the localized regime where eigenstates resemble product states. Near the transition, increased entanglement limits its applicability. Unitary tensor network approaches [11–13] represent the diagonalizing transformation U as a tensor network, providing access to all eigenstates simultaneously. These methods exploit the finite-depth circuit structure of U in the MBL phase but rely on local optimization schemes that can become trapped in local minima, and their accuracy degrades as the system approaches the ergodic-to-MBL transition.

Continuous unitary transformations (CUTs) [20, 21] offer an alternative by letting the Hamiltonian flow toward a diagonal form via coupled differential equations.

However, this system of equations is not closed, and the number of terms proliferates during the flow, necessitating truncation schemes [22, 23]. The recently developed Tensor Flow Equations (TFE) [24, 25] use an expansion in interaction strength, yielding promising results for weakly interacting systems but becoming less accurate at strong correlations. Previous attempts to combine tensor networks with CUTs include time-evolving block decimation (TEBD)-based approaches [26] and Baker-Campbell-Hausdorff (BCH)-based unitary tensor networks [27]. However, obtaining the complete spectrum with controlled accuracy using tensor-network-based flow equations has remained out of reach.

In this work, we present variational continuous unitary transformations (VCUTs), a method that combines tensor network representations with Wegner-Wilson flow equations using the time-dependent variational principle (TDVP) algorithm [28, 29]. Unlike TEBD, TDVP naturally handles the long-range interactions generated during the flow. By representing the diagonalizing unitary as a matrix product operator (MPO) with controlled bond dimension, VCUTs provides an optimized truncation scheme based on entanglement, enabling access to the entire spectrum with controlled accuracy.

We benchmark VCUTs against ED and TFE for system sizes $L \leq 16$, demonstrating accurate approximation of the full spectrum across the ergodic-to-localized crossover. The method maintains accuracy for system sizes up to $L = 48$, well beyond the reach of ED. Furthermore, VCUTs provides direct access to the dynamics of the diagonalizing unitary transformation and the spreading of local operators, offering real-space resolved insights into the localization transition. We observe that spatially localized regions of high entanglement persist deep into the localized regime, concentrated at bonds with small local disorder gradient Δh_i , directly reflecting the resonance structure of the MBL phase, and reliably identify LIOMs in this regime.

The paper is organized as follows: Section II introduces the model, and Section III describes the VCUTs method. Results are presented in Section IV, followed by a discussion in Section VII.

II. THE MODEL

We study the disordered spin- $\frac{1}{2}$ XXZ chain with open boundary conditions, a paradigmatic model for investigating many-body localization. The Hamiltonian reads

$$\mathcal{H} = \sum_{j=1}^{L-1} J_0 (S_j^x S_{j+1}^x + S_j^y S_{j+1}^y + \Delta S_j^z S_{j+1}^z) + \sum_{j=1}^L h_j S_j^z, \quad (2)$$

where J_0 is the exchange coupling, Δ controls the interaction anisotropy, and the on-site fields h_j are drawn independently from a uniform distribution $h_j \in [-W, W]$ with disorder strength W . Throughout this work, we set $J_0 = 1$ and $\Delta = 0.5$.

The isotropic case $\Delta = 1$ corresponds to the random-field Heisenberg chain (RFHC), a canonical model for MBL with the ergodic-to-MBL transition previously estimated at critical disorder strength $W_c \approx 3.7$ [8, 14, 30–32]. The critical disorder depends on the interaction strength Δ [33]: weaker interactions bring the system closer to the non-interacting Anderson localized limit, such that for $\Delta = 0.5$ the transition is expected at a lower value of W_c . We note, however, that finite-size effects in numerical studies remain a concern. The observation of slow dynamics toward delocalization deep in the putative MBL phase has raised questions about the stability of the MBL phase in the thermodynamic limit [34–36].

III. THE METHOD

A. Continuous unitary transformations

Continuous unitary transformations (CUTs) provide a framework for diagonalizing quantum Hamiltonians by flowing them toward diagonal form [20, 21]. The flow is governed by the differential equation

$$\frac{d\mathcal{H}(l)}{dl} = [\eta(l), \mathcal{H}(l)], \quad (3)$$

where l is the flow parameter and $\eta(l)$ is an anti-Hermitian generator. The formal solution is given by

$$\mathcal{H}(l) = U(l)\mathcal{H}(0)U^\dagger(l), \quad (4)$$

with $U(l) = \mathcal{T}_l \exp\left(-\int_0^l \eta(l') dl'\right)$, where \mathcal{T}_l denotes flow-ordering. A common choice is the Wegner generator [20],

$$\eta(l) = [\mathcal{H}_d(l), \mathcal{H}_{od}(l)], \quad (5)$$

where $\mathcal{H}_d(l)$ and $\mathcal{H}_{od}(l)$ denote the diagonal and off-diagonal parts of the Hamiltonian, respectively, as illustrated in Fig. 1(b). This choice guarantees that the off-diagonal norm decreases monotonically, driving the Hamiltonian toward diagonal form as $l \rightarrow \infty$. Once the flow converges, the eigenvalues can be read off from the diagonal elements of $\mathcal{H}(l)$, and the diagonalizing unitary $U(l)$ connects eigenstates to the computational basis.

B. Tensor network formulation of the flow

The key idea of VCUTs is to represent the flowing Hamiltonian $\mathcal{H}(l)$ as a matrix product operator (MPO) and solve the flow equation (3) using tensor network techniques. At each infinitesimal flow step, the Hamiltonian evolves according to

$$\mathcal{H}(l + dl) = e^{\eta(l)dl} \mathcal{H}(l) e^{-\eta(l)dl}. \quad (6)$$

To cast this into a form amenable to standard MPS time-evolution algorithms, we vectorize the MPO by combining the bra and ket indices at each site into a single index

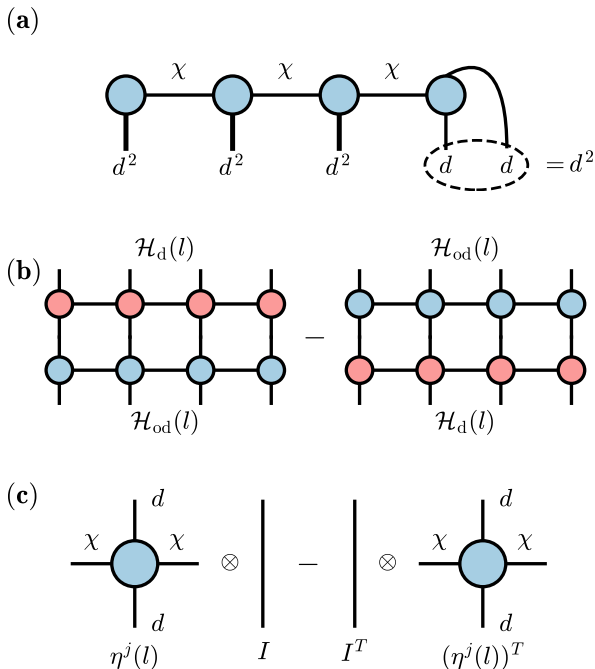


FIG. 1. Tensor network representation of the VCUTs method. (a) Vectorization of an MPO into an MPS by combining the bra and ket physical indices at each site into a single index of dimension d^2 . (b) Construction of the Wegner generator $\eta(l) = [\mathcal{H}_d(l), \mathcal{H}_{od}(l)]$ as the commutator of the diagonal and off-diagonal parts of the Hamiltonian. (c) The local superoperator $\mathcal{U}^j(l)$ from Eq. (8).

of dimension d^2 , yielding a matrix product state (MPS) representation of the vectorized Hamiltonian. This vectorization technique is analogous to that used for matrix product density operators (MPDOs) [37–40]. Formally, we map $\mathcal{H}(l) \mapsto |\mathcal{H}(l)\rangle\rangle$, as illustrated in Fig. 1(a). This vectorization transforms Eq. (6) into a Schrödinger-like equation,

$$\frac{d|\mathcal{H}(l)\rangle\rangle}{dl} = \mathcal{U}(l)|\mathcal{H}(l)\rangle\rangle, \quad (7)$$

where $\mathcal{U}(l)$ is a superoperator that acts on the vectorized Hamiltonian. The local tensor components of $\mathcal{U}(l)$ on site j are given by

$$\mathcal{U}^j(l) = \eta^j(l) \otimes I - I \otimes (\eta^j(l))^T, \quad (8)$$

where $\eta^j(l)$ is the local tensor of the Wegner generator defined in Eq. (5), as shown graphically in Fig. 1(c). The superoperator $\mathcal{U}(l)$ can itself be represented as an MPO acting on the enlarged local Hilbert space of dimension d^2 ; we refer to this as a super-MPO (SMPO) [37–40].

To solve Eq. (7), we employ the time-dependent variational principle (TDVP) algorithm, which provides a stable and efficient framework for time-evolving MPS [28, 29]. Since the superoperator $\mathcal{U}(l)$ is generally non-Hermitian, we employ the Krylov-Arnoldi algorithm to compute the required matrix exponentials [41, 42].

C. Diagonalizing unitary and local integrals of motion

Beyond the eigenvalue spectrum, VCUTs provides direct access to the diagonalizing unitary $U(l)$ and the local integrals of motion (LIOMs).

a. Diagonalizing unitary.—To construct the diagonalizing unitary $U(l)$ within the tensor network framework, we start from the MPO representation of the identity operator

$$I = \sum_{\sigma} |\sigma\rangle\langle\sigma|, \quad (9)$$

where the sum runs over all computational basis states $\sigma = (\sigma_1, \dots, \sigma_L)$. The identity MPO has bond dimension 1 with local tensors $\delta_{\sigma_j\sigma'_j}$. We vectorize this MPO into an MPS representation $|I\rangle\rangle$ and evolve it alongside the Hamiltonian using the same TDVP setup. At each infinitesimal step, $U(l)$ updates via left multiplication by $e^{\eta(l)dl}$. In the vectorized representation, this is implemented using a modified superoperator with local components

$$\mathcal{U}_U^j(l) = \eta^j(l) \otimes I, \quad (10)$$

yielding the vectorized diagonalizing unitary $|U(l)\rangle\rangle$.

b. Local integrals of motion.—In the MBL phase, the LIOMs τ_j^z are quasilocal operators that commute with each other and with the Hamiltonian [9, 43]. They are related to the bare spin operators by the diagonalizing unitary,

$$\tau_j^z = U^\dagger \sigma_j^z U. \quad (11)$$

Once the flow converges and the final diagonalizing unitary U is obtained, we compute the LIOMs by applying U to the MPO representation of the bare spin operator σ_j^z .

D. Implementation details

In our implementation, we represent the vectorized Hamiltonian with a maximum bond dimension D_H . The Wegner generator $\eta(l)$ is represented as an MPO with bond dimension $D_\eta = D_H$, as illustrated in Fig. 1(b). The diagonalizing unitary $U(l)$ requires a slightly larger bond dimension to maintain accuracy throughout the flow, and we use $D_U = D_H + 8$. To assess convergence with respect to bond dimension, we test $D_H = 16, 32, 48$ in our benchmarks.

The progress of the flow is monitored via the off-diagonal variance

$$V(l) = \frac{1}{2L} \sum_{i \neq j} |\mathcal{H}_{ij}(l)|^2, \quad (12)$$

which can be computed efficiently using tensor network contractions. The flow is terminated when the variance

decreases below a threshold $V(l) < 10^{-5}V(0)$ relative to the initial variance, or when the variance decrease stalls (less than 0.05% reduction over 20 consecutive steps).

We employ an adaptive time-stepping scheme that dynamically adjusts the flow step dl based on the variance reduction per step. At each step, the algorithm tests three candidate step sizes ($0.9dl$, dl , $1.1dl$) in parallel and selects the one yielding optimal variance reduction. The target is a variance drop of 1–3% per step: if the drop exceeds 3%, the step size is reduced by a factor of 0.8; if below 1%, it is increased by a factor of 1.2.

The TDVP algorithm introduces several sources of error [29]: (i) projection error arising from the finite bond dimension of the MPS ansatz, (ii) time-step error of order $\mathcal{O}(dl^3)$ per step from the second-order integrator, (iii) truncation error from bond dimension reduction in TDVP2, and (iv) local solver error from the numerical computation of matrix exponentials. For the local solver, we use the Krylov-Arnoldi algorithm with tolerance 10^{-12} , Krylov dimension 20–40 (scaled with system size) rendering the solver error negligible. We adopt a two-stage approach: initially, we use two-site TDVP to allow the bond dimension to grow dynamically as the flow progresses. Once the bond dimension reaches the specified cutoff D_H , we switch to one-site TDVP for the remainder of the flow. This hybrid strategy balances flexibility in capturing the growing entanglement with the computational efficiency and stability of single-site updates. The dominant sources of error are therefore projection error and time-step error, which we can control through careful selection of D_H and adaptive time-stepping.

For computing the autocorrelation function, the transformed states $|\psi_n\rangle = U|n\rangle$ obtained from VCUTs are generally non-orthogonal. To extract proper eigenstates, we solve the generalized eigenvalue problem $H_{mn}c_k^{(n)} = E_k S_{mn}c_k^{(n)}$, where $H_{mn} = \langle\psi_m|\mathcal{H}|\psi_n\rangle$ and $S_{mn} = \langle\psi_m|\psi_n\rangle$ are the Hamiltonian and overlap matrices. We orthogonalize using Cholesky decomposition of the overlap matrix $S = LL^T$, which is equivalent to Gram-Schmidt orthogonalization, transforming to $\tilde{H} = L^{-1}H(L^{-1})^T$ and solving the standard eigenvalue problem.

IV. RESULTS

We benchmark VCUTs on the disordered XXZ chain defined in Eq. (2) with $\Delta = 0.5$. The implementation parameters are specified in Section III D.

A. Full spectrum in the localized regime

We first compare the eigenenergies obtained by VCUTs with exact diagonalization (ED). Within VCUTs, the eigenenergies are read directly from the diagonal elements of the flowed Hamiltonian. In Fig. 3, we show

results for a single disorder realization with $L = 8$ and $W = 6$. The left panel displays all 70 eigenstates in the zero magnetization sector, while the right panel provides a magnified view of the energy levels near zero. The VCUTs results agree well with ED throughout the spectrum.

Next, we quantitatively benchmark VCUTs against ED and Tensor Flow Equations (TFE), another CUTs-based method capable of accessing the full spectrum. TFE has been successfully applied to finite-size quantum many-body systems, in some cases reaching sizes beyond ED [24, 25, 44]. For comparison, we use TFE with the exact same implementation as in Ref. [25]; for details see Appendix B. To quantify the accuracy, we define the relative energy error for each eigenstate $|j\rangle$ as

$$\epsilon_{\text{ED}}^{(j)} = \left| \frac{E_{\text{VCUTs}}^{(j)} - E_{\text{ED}}^{(j)}}{E_{\text{ED}}^{(j)}} \right|, \quad (13)$$

and compute the median error over all eigenstates in the zero magnetization sector,

$$\text{med}(\epsilon_{\text{ED}}) \equiv \text{med}_j(\epsilon_{\text{ED}}^{(j)}).$$

In Fig. 2, we compare the median errors for TFE and VCUTs across a range of disorder strengths. For $L = 8$ [panel (a)], VCUTs with bond dimension $D_H = 16$ already outperforms TFE for all values of W . Increasing the bond dimension to $D_H = 48$ further improves the accuracy, with the most significant gains observed in the localized regime at large W . The same comparison at $L = 16$ [panel (b)] confirms that VCUTs maintains its advantage over TFE at larger system sizes, with the error consistently a factor of 2–3 smaller across all disorder strengths. This is despite TFE employing a state-of-the-art generator optimized for the small-disorder regime [25], whereas VCUTs uses only the standard Wegner generator. To assess the scalability of VCUTs, we examine the variance suppression across different system sizes. In Fig. 2(c), we show both the initial variance $V(0)$ and the final variance $V(l_{\text{final}})$ as a function of L for several disorder strengths. The initial variance grows linearly with system size, $V(0) \propto L$, reflecting the extensive number of off-diagonal terms in the Hamiltonian. The final variance remains orders of magnitude smaller than $V(0)$ across all system sizes and disorder strengths, demonstrating that the Hamiltonian is approximately diagonalized even for $L = 48$, well beyond the reach of ED.

B. Entanglement structure of the flow

A key feature of MBL systems is that the diagonalizing unitary U can be represented as a finite-depth quantum circuit [45, 46], implying an efficient MPO representation with bounded bond dimension. In VCUTs, the full

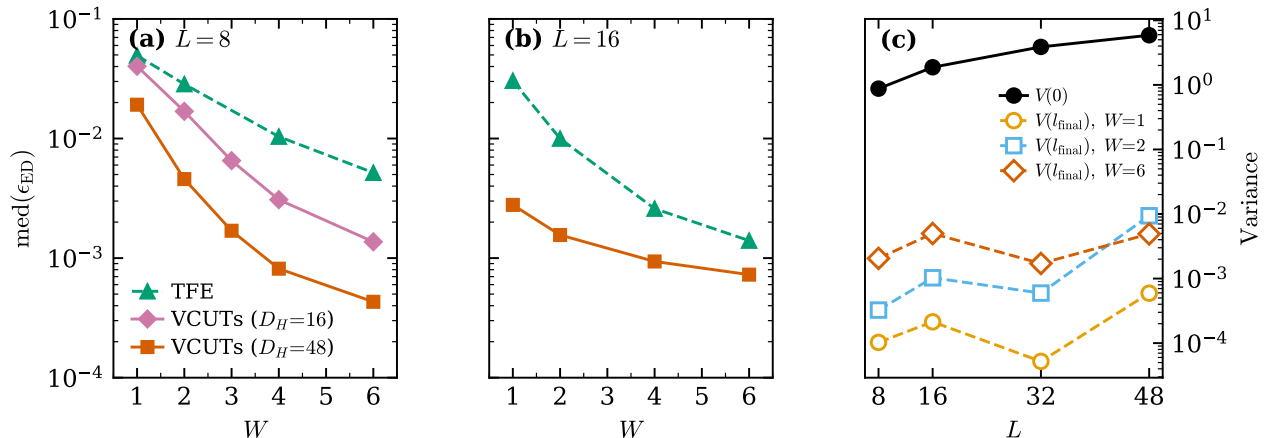


FIG. 2. Mean of the median relative energy error with respect to ED as a function of disorder strength W [panels (a) and (b)], and variance suppression as a function of system size L [panel (c)]. (a) $L = 8$: TFE (triangles), VCUTs with $D_H = 16$ (diamonds) and $D_H = 48$ (squares), averaged over 50 disorder realizations. (b) $L = 16$: TFE (triangles) and VCUTs with $D_H = 48$ (squares), averaged over 30 disorder realizations. (c) Initial variance $V(0)$ (black circles, solid line) and final variance $V(l_{\text{final}})$ (open markers, dashed lines) as a function of system size L for disorder strengths $W = 1, 2, 6$. For $L = 8$, $D_H = 32$, averaged over 49 disorder realizations; for $L = 16$, $D_H = 48$, averaged over 30 realizations; for $L = 32$ and 48, $D_H = 32$, a single realization is shown.

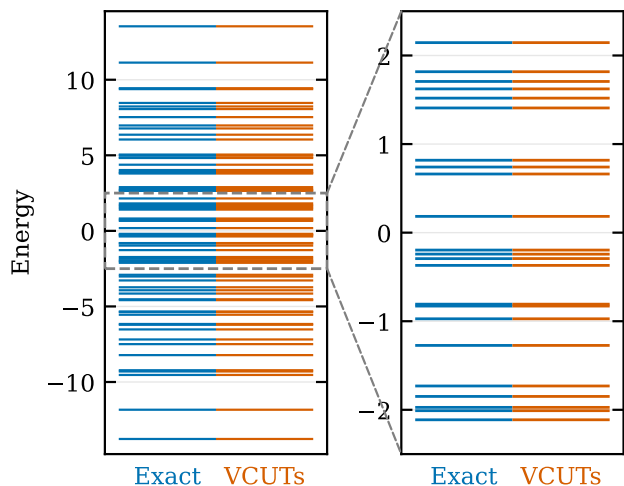


FIG. 3. Comparison between exact eigenenergies (blue lines) and energies obtained via VCUTs (red lines) for a system with $L = 8$ and $W = 6$. The left panel shows all 70 eigenstates in the zero magnetization sector. The right panel displays a magnified view of the energy levels near zero.

unitary is constructed as a product of infinitesimal transformations,

$$U(l) = \prod_{l'=0}^l e^{\eta(l')dl'} \equiv \prod_{l'=0}^l dU(l'), \quad (14)$$

where each $dU(l') = e^{\eta(l')dl'}$ is an MPO. To compute $dU(l')$, we apply the superoperator from Eq. (10) with the generator $\eta(l')$ and step size dl' to the identity oper-

ator, using TDVP2 with a truncation threshold of 10^{-4} . The entanglement structure of these infinitesimal generators provides insight into the spatial organization of the flow.

In Fig. 4, we show the bond entropy S^U of the diagonalizing unitary $U(l)$ as a function of bond index and flow step for $L = 48$ and $W = 12$, deep in the MBL phase. The entropy S^U grows predominantly at bonds where the local disorder gradient $\Delta h_i = |h_i - h_{i+1}|$ is small (blue-shaded regions), corresponding to near-resonant pairs of neighboring sites. These bonds are the first to accumulate entanglement as the flow progresses, forming a high-entropy core (enclosed by the red contour). To delineate this core we use the finite-size estimate $h_c \approx 2$ for the critical disorder gradient as a resonance criterion: bonds with $\Delta h_i < h_c$ are classified as near-resonant (red points in the top panel). We then set the entropy threshold S_{min}^U to the lowest bond entropy among these near-resonant bonds at the final flow step, and define the “bubble” as the connected region where $S^U \geq S_{\text{min}}^U$. In the top panel, bonds with $\Delta h_i > h_c$ that nonetheless lie inside the bubble are marked in orange: although initially off-resonant, their bond entropy exceeds the threshold, indicating that they have been “heated” by the adjacent high-entropy resonant (red) bonds. Bonds with $\Delta h_i > h_c$ outside the bubble (blue points) remain largely unaffected. This spatial selectivity confirms that the entanglement generated during the VCUT flow is governed by the local resonance structure of the disorder landscape, providing a direct real-space picture of where the emergent integrals of motion are localized.

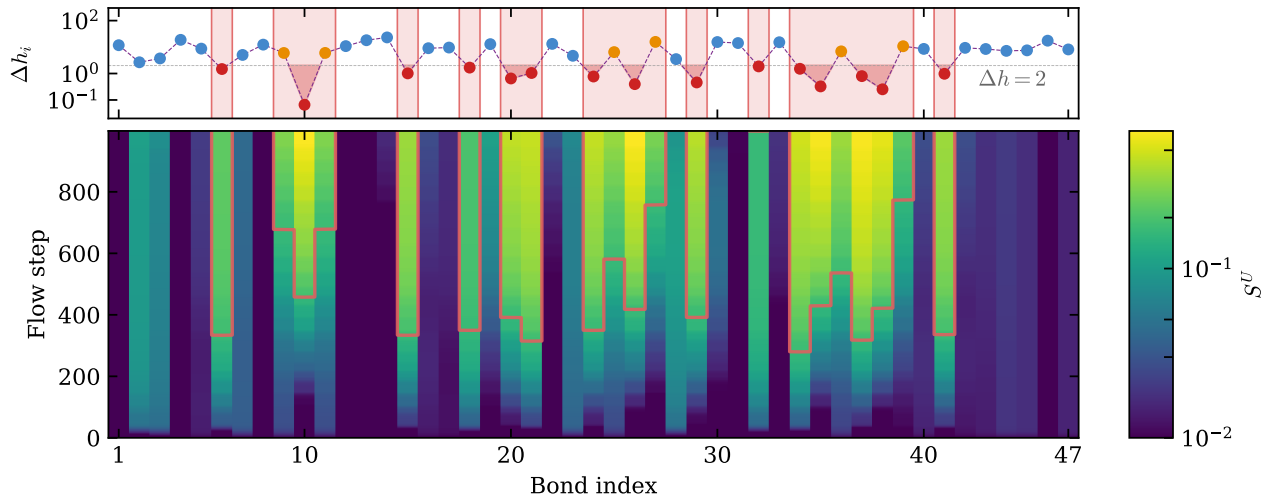


FIG. 4. Spatially resolved bond entropy S^U of the diagonalizing unitary $U(l)$ during the VCUTs flow for $L = 48$, $W = 12$ (single disorder realization, $D_H = 48$). *Main panel*: S^U on a logarithmic color scale as a function of bond index (horizontal) and flow step (vertical). The red contour encloses the high-entropy core ($S^U \geq S^U_{\min}$, where the threshold is set adaptively from the minimum final S^U among bonds with $\Delta h_i < 2$). Blue shading marks bonds where $\Delta h_i < 2$. *Top panel*: local disorder gradient $\Delta h_i = |h_i - h_{i+1}|$ at each bond; scatter points are colored red (below Δh threshold), orange (above threshold but inside the entropy core), or blue (above threshold and outside the core). The entropy accumulates preferentially at low- Δh bonds, revealing the resonance-driven spatial structure of the flow.

V. REAL TIME DYNAMICS

Having established that VCUTs accurately reproduces the eigenenergies, we now investigate its ability to capture real-time dynamics through the autocorrelation function. The dynamical autocorrelation of a local operator provides a direct probe of the localization properties of the system and serves as a stringent test of the quality of the LIOMs obtained from the diagonalizing unitary.

We compute the infinite-temperature autocorrelation function of the σ^z operator located at the middle site $j = L/2$:

$$C(t) = \frac{1}{2L} \text{Tr} [\sigma_j^z(t) \sigma_j^z(0)], \quad (15)$$

where $\sigma_j^z(t) = e^{i\mathcal{H}t} \sigma_j^z e^{-i\mathcal{H}t}$. Using the LIOM representation $\tau_j^z = U^\dagger \sigma_j^z U$ obtained from VCUTs, the autocorrelation can be computed efficiently. For comparison, we also compute the autocorrelation using ED (which provides the exact result) and TFE.

In Fig. 5, we show the disorder-averaged autocorrelation for $L = 8$ at three representative disorder strengths spanning the ergodic-to-MBL crossover. At early times ($t \lesssim 10$), both VCUTs and TFE show excellent agreement with the exact ED results across all disorder strengths. This demonstrates that the LIOMs obtained from both methods accurately capture the short-time dynamics, which is governed by the local structure of the operators.

The long-time behavior reveals an interesting dependence on disorder strength. In the ergodic regime ($W =$

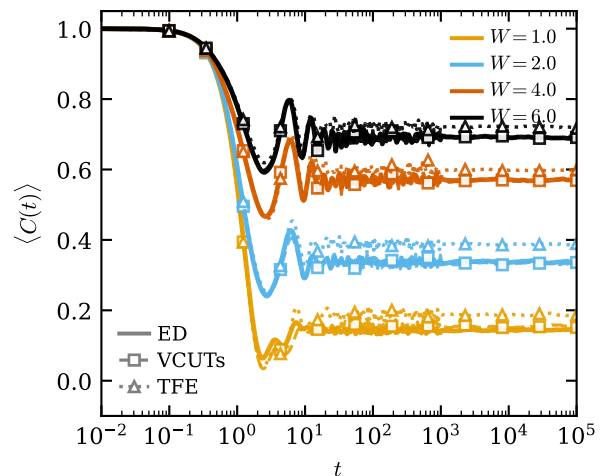


FIG. 5. Disorder-averaged dynamical autocorrelation $\langle C(t) \rangle$ for $L = 8$ and three disorder strengths $W = 1, 2, 6$, averaged over 50 realizations. Solid lines: ED (exact). Dashed lines with square markers: VCUTs ($D_H = 48$). Dotted lines with triangle markers: TFE. Different colors correspond to different disorder strengths. A moving average is applied for $t > 1000$ to reduce oscillations. The autocorrelation is computed from the LIOM $\tau_{L/2}^z = U^\dagger \sigma_{L/2}^z U$ located at the middle site.

1), VCUTs maintains good agreement with ED even at longer times, demonstrating that the method captures the essential physics of the delocalized phase. At the crossover ($W = 2$) and in the localized regime ($W = 6$),

VCUTs and TFE exhibit similar long-time behavior, with the autocorrelation approaching a finite saturation value characteristic of localized systems.

However, subtle deviations between VCUTs/TFE and ED emerge at very long times in the crossover and localized regimes. This mismatch arises because the transformed states $|\psi_n\rangle = U|n\rangle$ obtained from VCUTs are not exactly orthogonal due to the finite bond dimension truncation. When computing the autocorrelation, these non-orthogonality effects accumulate over many eigenstates and manifest as deviations at long times. The Gram-Schmidt orthogonalization procedure described in Section III D mitigates but does not fully eliminate this effect, as it relies on the approximate overlap matrix computed from the truncated MPS. Nevertheless, VCUTs exhibits slightly better overall correspondence with ED compared to TFE, consistent with its non-perturbative treatment of interactions.

VI. INSIGHT ON THE ERGODIC-TO-LOCALIZATION CROSSOVER

A key signature of the ergodic-to-MBL transition is the behavior of eigenstate entanglement entropy [14, 47, 48]. In the ergodic phase, eigenstates exhibit volume-law entanglement consistent with the eigenstate thermalization hypothesis (ETH), while in the MBL phase, eigenstates follow an area law due to the localized nature of the LLOMs. Near the transition, the sample-to-sample fluctuation of the entanglement entropy develops a broad maximum, which has been proposed as a practical indicator of the crossover region and the critical disorder strength W_c [12, 49].

In Fig. 6, we compare the half-cut entanglement entropy statistics obtained from VCUTs with exact diagonalization for $L = 8$. The VCUT dressed states are generated by applying the diagonalizing unitary U from the flow to product states $|n\rangle$, $|\psi_n\rangle = U|n\rangle$. In panel (a), we plot the mean entanglement entropy $\langle S \rangle_{s,n} = \langle \langle S_{cs}^n \rangle_{c,s} \rangle_n$, where the half-chain entanglement entropy S_{cs}^n is first averaged over eigenstates s and spatial cuts c for each disorder realization n , and then averaged over realizations. In our case c runs over the three most central left-right bond cuts (the middle bond and its two nearest neighbors), which provides a robust estimate of the half-chain entanglement while remaining accessible from the MPS bond structure. $\langle S \rangle_{s,n}$ decreases monotonically with increasing disorder strength, reflecting the crossover from volume-law to area-law entanglement. In panel (b), we show the sample-to-sample fluctuation diagnostic $\Delta_S^{\text{samples}} = \sigma_n(\langle S_{cs}^n \rangle_{c,s})$, following Refs. [12, 49], where σ_n denotes the standard deviation across disorder realizations. $\Delta_S^{\text{samples}}$ thus quantifies how strongly the mean entanglement entropy varies from sample to sample at fixed disorder strength; a pronounced peak signals enhanced heterogeneity in the crossover regime.

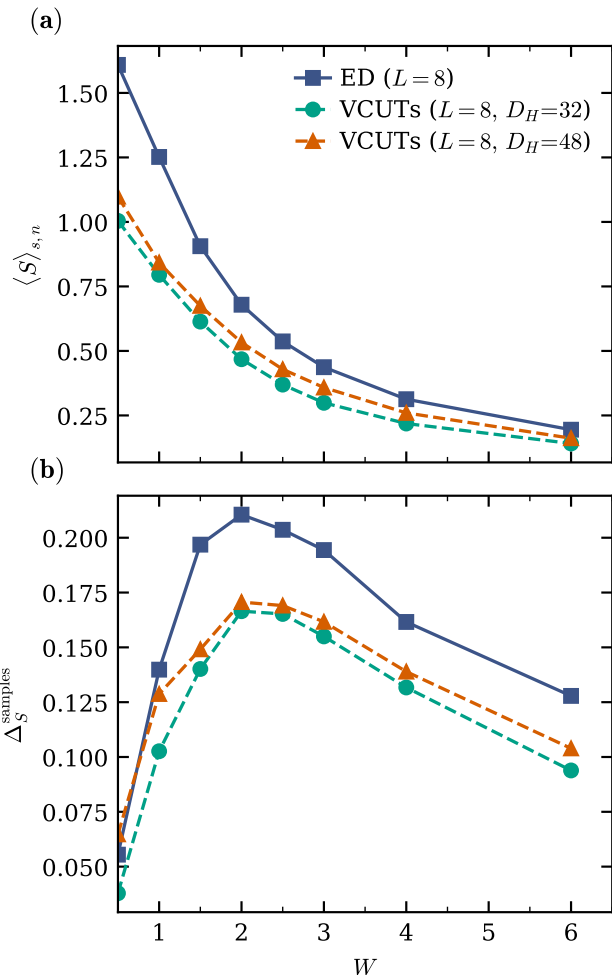


FIG. 6. Half-cut entanglement entropy statistics as a function of disorder strength W ; for each W we average over 50–100 disorder realizations. (a) Mean entanglement entropy $\langle S \rangle_{s,n}$ (defined in the text) from ED ($L = 8$) and VCUTs ($L = 8$, $D_H = 32, 48$). (b) Sample-to-sample fluctuation diagnostic $\Delta_S^{\text{samples}}$ (defined in the text) for ED ($L = 8$) and VCUTs ($L = 8$, $D_H = 32, 48$).

$\Delta_S^{\text{samples}}$ exhibits a broad maximum at intermediate disorder, as also observed in Refs. [12, 49]. For $L = 8$, ED and VCUTs both display a qualitatively similar peak in panel (b). The remaining deviations are most visible at low disorder, where entanglement is largest and finite bond dimension effects are strongest.

Importantly, increasing the bond dimension from $D_H = 32$ to $D_H = 48$ systematically improves the agreement with ED, particularly in the low-disorder regime where entanglement is largest. With $D_H = 48$, VCUTs captures the qualitative features of the crossover, including the peak position and the overall shape of the $\Delta_S^{\text{samples}}$ curve. This demonstrates that VCUTs can provide meaningful insights into the ergodic-to-MBL crossover, with accuracy that improves as the bond dimension is increased.

VII. DISCUSSION

We have developed variational continuous unitary transformations (VCUTs), a method that combines Wegner-Wilson flow equations with tensor network techniques to approximately diagonalize many-body Hamiltonians. By representing the flowing Hamiltonian as an MPO and employing TDVP for the integration, VCUTs provides a controlled truncation scheme based on entanglement that prevents the proliferation of terms inherent to conventional CUTs implementations. The bond dimension D_H serves as the single control parameter that governs the trade-off between accuracy and computational cost.

We benchmarked VCUTs on the disordered XXZ chain across the ergodic-to-MBL crossover. For small system sizes ($L = 8$), VCUTs accurately reproduces the full spectrum, outperforming the perturbative TFE approach for all disorder strengths. The method scales to system sizes up to $L = 48$, well beyond the reach of exact diagonalization, demonstrating the practical utility of the tensor network formulation.

Beyond eigenenergies, VCUTs provides direct access to the diagonalizing unitary U and the local integrals of motion. The spatially resolved bond entropy S^U of the diagonalizing unitary reveals that, deep in the MBL phase, the entanglement concentrates at bonds with small local disorder gradient Δh_i , identifying the near-resonant bonds that govern the spatial structure of the emerging LIOMs. This provides a direct real-space picture of the localization mechanism, consistent with the finite-depth circuit structure expected for MBL systems [11]. The LIOMs obtained from VCUTs accurately capture both short-time and long-time dynamics of the autocorrelation function, and the eigenstate entanglement entropy statistics provide insights into the ergodic-to-MBL crossover.

The main limitation of VCUTs lies in the ergodic regime, where the flow generates high entanglement that exceeds the capacity of the finite bond dimension. This manifests as reduced accuracy at small disorder and a mild shift of entanglement-based crossover diagnostics (such as the peak in $\Delta_S^{\text{samples}}$). Increasing the bond dimension systematically improves the results, suggesting that the method can be refined to capture the transition region more accurately.

Several directions for future improvement are apparent. First, the standard Wegner generator used here becomes inefficient near degeneracies; incorporating scrambling transformations [24] via a combination of Wegner and Toda-Mielke generators (Appendix A) could enhance performance in such cases. Second, advances in tensor network algorithms and high-performance computing would enable access to larger bond dimensions and system sizes. Finally, the formalism developed here—based on vectorized MPOs and TDVP evolution—is directly applicable to open quantum systems described by Lindblad master equations [37–40], an extension we are currently pursuing.

ACKNOWLEDGMENTS

This work was funded by the Deutsche Forschungsgemeinschaft (DFG, German Research Foundation) – 508440990. Simulations were performed with computing resources granted by RWTH Aachen University under project rwth1807 and rwth1543.

Appendix A: Tensor network representations for generators

In this appendix we describe the tensor network construction of the Wegner and Toda-Mielke generators used in continuous unitary transformations.

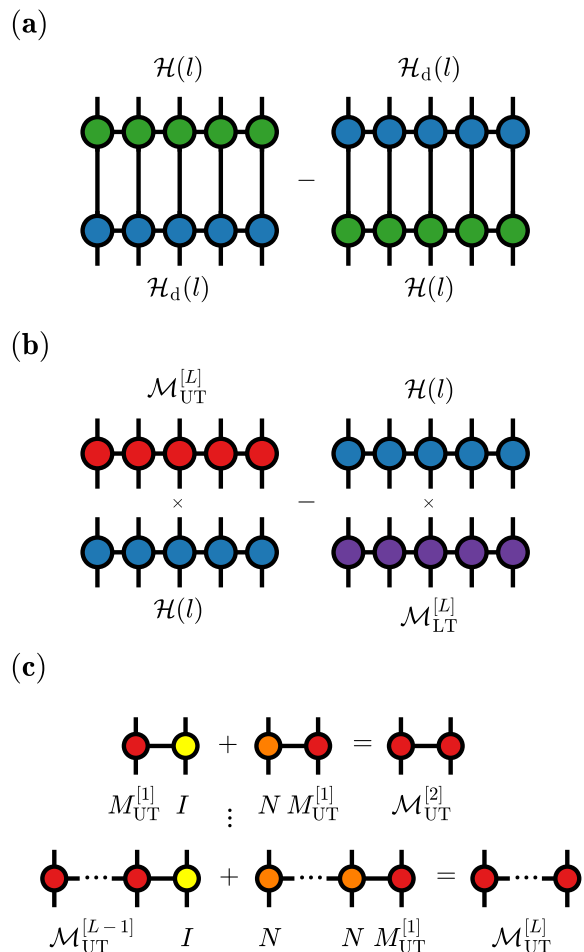


FIG. 7. Tensor network construction of flow generators. (a) Wegner generator $\eta_W(l) = [\mathcal{H}_d(l), \mathcal{H}(l)]$ computed as the difference of two MPO contractions. (b) Toda-Mielke generator $\eta_T(l)$ obtained via element-wise multiplication (denoted \times) of the Hamiltonian with upper and lower triangular mask tensors. (c) Iterative construction of the upper triangular mask tensor $\mathcal{M}_{UT}^{[L]}$ for a system of length L .

1. Wegner generator

The Wegner generator defined in Eq. (5) can be equivalently written as

$$\eta_W(l) = [\mathcal{H}_d(l), \mathcal{H}(l)], \quad (\text{A1})$$

since $[\mathcal{H}_d(l), \mathcal{H}_d(l)] = 0$. This form is more convenient for implementation because it requires only one commutator rather than explicitly separating $\mathcal{H}_{\text{od}}(l)$.

The diagonal part $\mathcal{H}_d(l)$ is obtained by setting all off-diagonal elements within each local $d \times d$ block of the physical indices to zero. The commutator is then computed using standard MPO arithmetic, as illustrated in Fig. 7(a). The resulting generator has bond dimension scaling as $2D^2$, where D is the bond dimension of the Hamiltonian MPO. To prevent memory growth during the flow, we apply variational compression [50, 51] to reduce the bond dimension, which also avoids artificial memory effects that can arise from SVD-based truncation.

2. Toda-Mielke generator

The Toda-Mielke generator [52] is defined as

$$\eta_T^{\alpha\beta}(l) = \text{sgn}(\beta - \alpha) \mathcal{H}_{\alpha\beta}(l), \quad (\text{A2})$$

which preserves the band structure of the Hamiltonian while lifting degeneracies. Unlike the Wegner generator, this requires constructing upper and lower triangular mask tensors in the many-body Hilbert space. We

use the 2×2 building blocks $I = \begin{bmatrix} 1 & 0 \\ 0 & 1 \end{bmatrix}$, $N = \begin{bmatrix} 1 & 1 \\ 1 & 1 \end{bmatrix}$, and $M_{\text{UT}} = \begin{bmatrix} 0 & 1 \\ 0 & 0 \end{bmatrix}$. The upper triangular mask tensor $\mathcal{M}_{\text{UT}}^{[L]}$ is constructed iteratively as shown in Fig. 7(c), and the lower triangular mask $\mathcal{M}_{\text{LT}}^{[L]}$ follows analogously. Both masks are highly compressible to bond dimension $D = 2$, independent of system size L . The Toda-Mielke generator is then obtained by element-wise multiplication of $\mathcal{H}(l)$ with these masks [Fig. 7(b)]; details on element-wise MPO multiplication can be found in Ref. [53].

Appendix B: Tensor Flow Equations (TFE)

TFE and VCUTs are both based on Wegner's flow equations but differ in their operator representation and truncation scheme. In TFE, operators are expanded and truncated to a specified order in the interaction strength U , yielding a resummed perturbative expansion that is most accurate at weak interactions. For the TFE simulations presented in this work, we run the flow using a combination of scrambling and Wegner generators until $l = 1000$ or until the convergence criteria $\max |\mathcal{H}_{\text{off}}^{(2)}(l)| < 10^{-6}$ and $\max |\mathcal{H}_{\text{off}}^{(4)}(l)| < 10^{-4}$ are satisfied, where $\mathcal{H}_{\text{off}}^{(2),(4)}(l)$ denote the remaining off-diagonal elements in the one- and two-particle sectors, respectively, as introduced in Ref. [25]. Since TFE is formulated for fermionic operators, a Jordan-Wigner transformation is applied to express Eq. (2) in terms of interacting spinless fermions.

* qiyu.liu@tu-braunschweig.de
 † dante.kennes@rwth-aachen.de
 ‡ c.karrasch@tu-braunschweig.de

- [1] L. Fleishman and P. W. Anderson, Interactions and the anderson transition, *Physical Review B* **21**, 2366 (1980).
- [2] D. Basko, I. Aleiner, and B. Altshuler, Metal-insulator transition in a weakly interacting many-electron system with localized single-particle states, *Annals of Physics* **321**, 1126 (2006).
- [3] I. V. Gornyi, A. D. Mirlin, and D. G. Polyakov, Interacting electrons in disordered wires: Anderson localization and low- T transport, *Physical Review Letters* **95**, 206603 (2005).
- [4] R. Nandkishore and D. A. Huse, Many-body localization and thermalization in quantum statistical mechanics, *Annual Review of Condensed Matter Physics* **6**, 15 (2015).
- [5] D. A. Abanin, E. Altman, I. Bloch, and M. Serbyn, Colloquium : Many-body localization, thermalization, and entanglement, *Reviews of Modern Physics* **91**, 021001 (2019).
- [6] M. Žnidarič, T. Prosen, and P. Prelovšek, Many-body localization in the heisenberg XXZ -magnet in a random field, *Physical Review B* **77**, 064426 (2008).
- [7] V. Oganesyan and D. A. Huse, Localization of interacting fermions at high temperature, *Physical Review B* **75**, 155111 (2007).
- [8] A. Pal and D. A. Huse, Many-body localization phase transition, *Physical Review B* **82**, 174411 (2010).
- [9] V. Ros, M. Müller, and A. Scardicchio, Integrals of motion in the many-body localized phase, *Nuclear Physics B* **891**, 420 (2015).
- [10] M. Serbyn, Z. Papić, and D. A. Abanin, Criterion for many-body localization-delocalization phase transition, *Physical Review X* **5**, 041047 (2015).
- [11] F. Pollmann, V. Khemani, J. I. Cirac, and S. L. Sondhi, Efficient variational diagonalization of fully many-body localized hamiltonians, *Phys. Rev. B* **94**, 041116 (2016).
- [12] T. B. Wahl, A. Pal, and S. H. Simon, Efficient representation of fully many-body localized systems using tensor networks, *Physical Review X* **7**, 021018 (2017).
- [13] D. Pekker, B. K. Clark, V. Oganesyan, and G. Refael, Fixed points of wegner-wilson flows and many-body localization, *Physical Review Letters* **119**, 075701 (2017).
- [14] D. J. Luitz, N. Laflorencie, and F. Alet, Many-body localization edge in the random-field heisenberg chain, *Physical Review B* **91**, 081103 (2015).

- [15] D. J. Luitz and Y. B. Lev, The ergodic side of the many-body localization transition, *Annalen der Physik* **529**, 00350 (2017).
- [16] E. Altman and R. Vosk, Universal dynamics and renormalization in many-body-localized systems, *Annual Review of Condensed Matter Physics* **6**, 383 (2015).
- [17] E. H. Lieb and D. W. Robinson, The finite group velocity of quantum spin systems, *Commun. Math. Phys.* **28**, 251 (1972).
- [18] F. Pietracaprina, N. Macé, D. J. Luitz, and F. Alet, Shift-invert diagonalization of large many-body localizing spin chains, *SciPost Physics* **5**, 045 (2018).
- [19] V. Khemani, F. Pollmann, and S. L. Sondhi, Obtaining highly excited eigenstates of many-body localized hamiltonians by the density matrix renormalization group approach, *Phys. Rev. Lett.* **116**, 247204 (2016).
- [20] F. J. Wegner, Flow equations for hamiltonians, *Nuclear Physics B - Proceedings Supplements* **90**, 141 (2000).
- [21] S. Kehrein, *The Flow Equation Approach to Many-Particle Systems* (Springer Berlin Heidelberg, 2006).
- [22] T. Fischer, S. Duffé, and G. S. Uhrig, Adapted continuous unitary transformation to treat systems with quasiparticles of finite lifetime, *New Journal of Physics* **12**, 033048 (2010).
- [23] S. J. Thomson and M. Schiró, Time evolution of many-body localized systems with the flow equation approach, *Physical Review B* **97**, 060201 (2018).
- [24] S. J. Thomson and J. Eisert, Unraveling long-time quantum dynamics using flow equations, *Nature Physics* **20**, 1401–1406 (2024).
- [25] J.-N. Herre, Q. Liu, R. Rausch, C. Karrasch, and D. M. Kennes, Investigating stark mbl with continuous unitary transformation flows (2024).
- [26] S. Sahin, K. P. Schmidt, and R. Orús, Entanglement continuous unitary transformations, *Europhysics Letters* **117**, 20002 (2017).
- [27] X. Yu, D. Pekker, and B. K. Clark, Bulk geometry of the many body localized phase from wilson-wegner flow, prePrint (2019), arXiv:1909.11097 [cond-mat.str-el].
- [28] J. Haegeman, J. I. Cirac, T. J. Osborne, I. Pižorn, H. Verschelde, and F. Verstraete, Time-dependent variational principle for quantum lattices, *Physical Review Letters* **107**, 070601 (2011).
- [29] J. Haegeman, C. Lubich, I. Oseledets, B. Vandereycken, and F. Verstraete, Unifying time evolution and optimization with matrix product states, *Phys. Rev. B* **94**, 165116 (2016).
- [30] J. Šuntajs, J. Bonča, T. c. v. Prosen, and L. Vidmar, Ergodicity breaking transition in finite disordered spin chains, *Phys. Rev. B* **102**, 064207 (2020).
- [31] J. Šuntajs, J. Bonča, T. c. v. Prosen, and L. Vidmar, Quantum chaos challenges many-body localization, *Phys. Rev. E* **102**, 062144 (2020).
- [32] J. Colbois, F. Alet, and N. Laflorencie, Interaction-driven instabilities in the random-field xxz chain, *Phys. Rev. Lett.* **133**, 116502 (2024).
- [33] M. Hopjan and L. Vidmar, Interaction-driven instabilities in the random-field XXZ chain, arXiv preprint (2024), arXiv:2403.09608 [cond-mat.dis-nn].
- [34] F. Weiner, F. Evers, and S. Bera, Slow dynamics and strong finite-size effects in many-body localization with random and quasiperiodic potentials, *Phys. Rev. B* **100**, 104204 (2019).
- [35] E. V. H. Doggen, F. Schindler, K. S. Tikhonov, A. D. Mirlin, T. Neupert, D. G. Polyakov, and I. V. Gornyi, Many-body localization and delocalization in large quantum chains, *Phys. Rev. B* **98**, 174202 (2018).
- [36] G. Zisling, D. M. Kennes, and Y. Bar Lev, Transport in stark many-body localized systems, *Physical Review B* **105**, 1140201 (2022).
- [37] M. Zwolak and G. Vidal, Mixed-state dynamics in one-dimensional quantum lattice systems: A time-dependent superoperator renormalization algorithm, *Phys. Rev. Lett.* **93**, 207205 (2004).
- [38] A. H. Werner, D. Jaschke, P. Silvi, M. Kliesch, T. Calarco, J. Eisert, and S. Montangero, Positive tensor network approach for simulating open quantum many-body systems, *Phys. Rev. Lett.* **116**, 237201 (2016).
- [39] J. c. v. Guth Jarkovský, A. Molnár, N. Schuch, and J. I. Cirac, Efficient description of many-body systems with matrix product density operators, *PRX Quantum* **1**, 010304 (2020).
- [40] H. Weimer, A. Kshetrimayum, and R. Orús, Simulation methods for open quantum many-body systems, *Rev. Mod. Phys.* **93**, 015008 (2021).
- [41] M. Hochbruck and C. Lubich, On krylov subspace approximations to the matrix exponential operator, *SIAM J. Numer. Anal.* **34**, 1911 (1997).
- [42] Y. Saad, *Numerical Methods for Large Eigenvalue Problems* (Manchester University Press, 1992).
- [43] M. Serbyn, Z. Papić, and D. A. Abanin, Local conservation laws and the structure of the many-body localized states, *Phys. Rev. Lett.* **111**, 127201 (2013).
- [44] S. J. Thomson and M. Schiró, Local integrals of motion in quasiperiodic many-body localized systems, *SciPost Physics* **14**, 125 (2023).
- [45] D. Pekker and B. K. Clark, Encoding the structure of many-body localization with matrix product operators, *Physical Review B* **95**, 035116 (2017).
- [46] D. Pekker, B. K. Clark, V. Oganesyan, and G. Refael, Fixed points of wegner-wilson flows and many-body localization, *Phys. Rev. Lett.* **119**, 075701 (2017).
- [47] J. A. Kjäll, J. H. Bardarson, and F. Pollmann, Many-body localization in a disordered quantum ising chain, *Phys. Rev. Lett.* **113**, 107204 (2014).
- [48] M. Serbyn, Z. Papić, and D. A. Abanin, Criterion for many-body localization-delocalization phase transition, *Phys. Rev. X* **5**, 041047 (2015).
- [49] V. Khemani, S. P. Lim, D. N. Sheng, and D. A. Huse, Critical properties of the many-body localization transition, *Phys. Rev. X* **7**, 021013 (2017).
- [50] U. Schollwöck, The density-matrix renormalization group in the age of matrix product states, *Ann. Phys.* **326**, 96 (2011).
- [51] J. van der Kolk, Time evolution of matrix product operators in the heisenberg picture, Phd thesis (2011).
- [52] Mielke, A., Flow equations for band-matrices*, *Eur. Phys. J. B* **5**, 605 (1998).
- [53] H. Shinaoka, M. Wallerberger, Y. Murakami, K. Nogaki, R. Sakurai, P. Werner, and A. Kauch, Multiscale space-time ansatz for correlation functions of quantum systems based on quantics tensor trains, *Physical Review X* **13**, 021015 (2023).